[American Journal of Science, Vol. 313, May, 2013, P. 490–515, DOI 10.2475/05.2013.03]

TRACING PALEOFLUID SOURCES USING CLUMPED ISOTOPE THERMOMETRY OF DIAGENETIC CEMENTS ALONG THE MOAB FAULT, UTAH

SARAH C. BERGMAN, KATHARINE W. HUNTINGTON†, and JULIET G. CRIDER

Department of Earth and Space Sciences, University of Washington, Box 351310, 4000 15th Avenue NE, Seattle, Washington, 98195-1310

ABSTRACT. Interactions among fluids, deformation structures, and chemical changes in sediments impact deformation of the shallow crust, influencing the preservation and extraction of the economic resources it contains. These interactions have been studied along the Moab Fault, in the Paradox Basin, Utah, where diagenetic cements, joints, cataclastic deformation bands and slip surfaces developed during faulting are thought to control fault permeability. Previous fluid inclusion micro-thermometry and stable isotopic data from calcite cements collected along segments of the Moab Fault suggest cements precipitated from hot basin fluids that migrated up the fault and interacted with a shallower meteoric groundwater source. In this study, we investigate the interactions of these fluids with deformation structures using clumped isotope thermometry of calcite cements along the Moab Fault. Guided by prior high-resolution mapping of deformation structures and calcite cements, we measured the growth temperature of calcite cements collected at varying distance from fault segments and fault intersections. Cement temperatures from individual segments vary greatly; cements along a relatively simple fault segment indicate temperatures ranging from 67 to 128 °C, similar to previously published fluid inclusion homogenization temperatures from a cement sample collected in the same locality, while a nearby fault intersection hosts cements with temperatures of 13 to 88 °C. The spatial pattern of cement temperatures revealed by clumped isotope thermometry suggests that intensely jointed zones associated with fault intersections enable rapid down-fault migration of cool surface waters and that deformation-band faults with their associated slip surfaces may further compartmentalize fluid flow, restricting fluid sources to warm waters thermally equilibrated with the country rock outside the jointed zone. Our data confirm that the relationship between faults and fluid flow can vary greatly over short length scales, and suggest that some fracture zones can be highly conductive to depths as great as 2 km.

Key words: Deformation structures, diagenesis, fluids, calcite cement, fault, Paradox Basin, clumped isotopes

INTRODUCTION

Brittle fault systems can serve as either conduits or barriers to fluid flow (for example, Caine and others, 1996; Davatzes and others, 2005), impacting mass and heat transfer in the crust and influencing the potential storage and migration of hydrocarbons and geothermal fluids. For fault systems in porous sandstones, two classes of structures control both hydrological and mechanical behavior during fault evolution: cataclastic deformation bands and joints. Deformation bands form tabular and anastomosing zones of localized deformation and crushed grains (Aydin and Johnson, 1978) and may evolve to host discrete slip surfaces (Aydin and Johnson, 1978; Fossen and others, 2007). Joints are planar fractures that show displacement normal to their surfaces and may experience subsequent shear that leads to brecciation (for example, Myers and Aydin, 2004; Davatzes and others, 2005). While deformation bands and subsequent slip surfaces typically reduce permeability within and across fault zones (Antonellini and Aydin, 1994), joints can act as significant conduits for fluid (for example, Long and others, 1996; Aydin, 2000).

† Corresponding author: kate1@uw.edu

The development of these structures during faulting in sandstones and their influence on fluid migration has been studied in detail along the Moab Fault, a large normal fault system in the Paradox Basin, Utah (Nuccio and Condon, 1996; Foxford and others, 1996, 1998; Chan and others, 2000; Davatzes and others, 2003, 2005; Johansen and others, 2005, 2008; Eichhubl and others, 2009). Recent work highlights the importance of both structures and diagenesis in controlling fluid migration in this and other large fault systems (Eichhubl and others, 2000, 2004, 2009; Davatzes and others, 2005; Fossen and others, 2005; Laubach and Ward, 2006; Laubach and others, 2009). Diagenetic cements precipitated along the Moab Fault preserve information about the origin and history of the diagenetic fluids from which they grew, and their abundance in areas of structural complexity led previous workers to infer that paleo-fluid flow was focused along highly jointed fault segments (Eichhubl and others, 2009).

These mapping results combined with fluid inclusion micro-thermometry and stable isotopic analysis of calcite cements from the Moab Fault suggest that joints served as conduits for the ascension of warm, saline basinal fluids that interacted with a shallower meteoric water source (Chan and others, 2000; Eichhubl and others, 2009). Chan and others (2000) envisioned this shallower, ^{18}O and ^{13}C-enriched end-member to be sourced from high-elevation meteoric precipitation, driven by topographic gradients to circulate deep in the basin, where it interacted with hydrocarbons from deeper stratigraphic levels to precipitate calcite cement at temperatures on the order of 50 or 25 °C. Subsequently, Eichhubl and others (2009) observed primary two-phase fluid inclusions from one sample indicating calcite cement growth temperatures of 84 to 125 °C. They interpreted these values to be consistent with topographically driven, deep circulation of meteoric water, with the higher range of temperatures representing focused flow of hot fluid up the fault zone, but lacked the data to investigate the relationship between fluid temperature and distance from the fault.

We complement previous work by using clumped isotope thermometry (Ghosh and others, 2006; Eiler, 2007) to document spatial variations in the temperature of the fluids from which calcite cements precipitated. Huntington and others (2011) used clumped isotopes to independently determine both the temperature and oxygen isotopic composition of the water ($\delta^{18}O_{H_2O}$) from which diagenetic cements from the Colorado Plateau grew, and Swanson and others (2012) applied the method to study conditions of cataclastic deformation along the Mormon Peak detachment in the Basin and Range, Nevada. We apply this technique for the first time to study the role of fault zone heterogeneity in controlling fluid flow in the shallow crust. Along joint-dominated fault segment 5 (fig. 1), we find high temperature cements, consistent with previous fluid inclusion microthermometry estimates and structural analysis indicating that the fault was a conduit for hot fluids (Eichhubl and others, 2009). However, near the intersection of fault segments 1 and 2—a zone characterized by both deformation bands and slip surfaces and abundant joints—we find a broad range of temperatures that vary systematically with distance from the fault and correlate with variations in secondary deformation structures, providing further evidence that these structures play an important role in transmission and compartmentalization of fluids in porous rocks.

STUDY AREA

The Moab Fault is a basin-scale normal fault cutting Pennsylvanian to Cretaceous sedimentary units in the Paradox Basin of the southwestern United States (fig. 1; Doelling, 1985; Foxford and others, 1996; Nuccio and Condon, 1996; Davatzes and Aydin, 2003; Davatzes and others, 2005). The Moab Fault was active between the Permian and mid-Tertiary, and the last significant fault motion has been dated at 50 to 60 Ma from K-Ar dates in fault zone illite, indicating faulting occurred near maximum

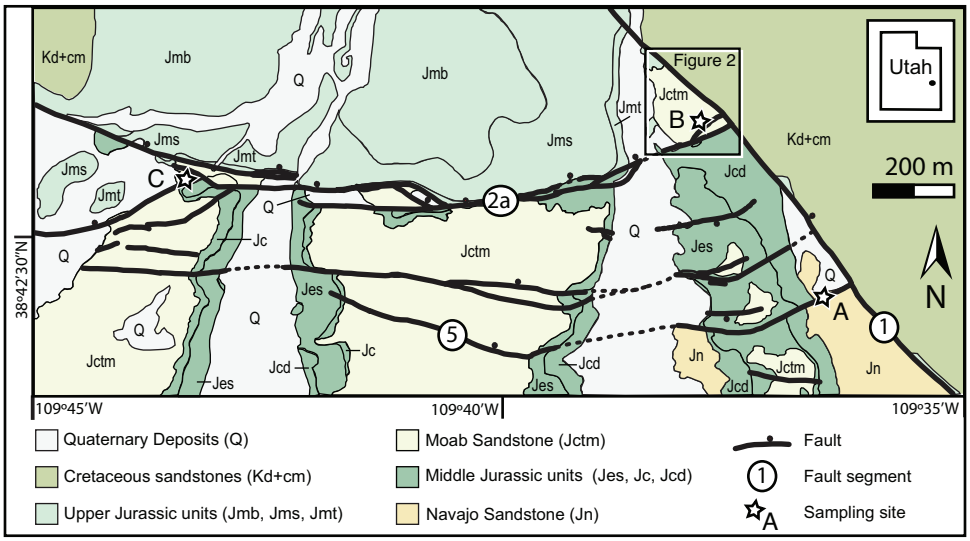

Fig. 1. (A) Geologic map of the Moab Fault system at Courthouse Rock redrawn and simplified from Davatzes and others (2005), and Eichhubl and others (2009). Fault segments referenced in the text are numbered following Davatzes and others (2005). Sampling sites are indicated by white stars. Unit symbols as follows: Kd + cm: Cretaceous Dakota and Cedar Mountain Formations, undifferentiated; Jmb, Jms, and Jmt: Brushy Basin, Salt Wash, and Tidwell Members of the Jurassic Morrison Formation; Jc, Jctm: Jurassic Curtis Formation and Moab Tongue Members; Jes: Slick Rock Member of the Jurassic Entrada Formation; Jcd: Dewey Bridge Member of the Jurassic Carmel Formation. Inset shows the approximate location of the study region in eastern Utah.

burial (Pevear and others, 1997). Both the structural evolution and diagenetic history of the Moab Fault system have been studied extensively (for example, Foxford and others, 1996, 1998; Pevear and others, 1997; Garden and others, 2001; Davatzes and Aydin, 2003; Davatzes and others, 2003, 2005; Johansen and others, 2005, 2008; Solum and others, 2005, 2010; Eichhubl and others, 2009). Our work builds on high resolution prior mapping (Davatzes and others, 2005; Johansen and others, 2005; Eichhubl and others, 2009) to examine the relationship between structural architecture and fault permeability with new paleotemperature determinations from clumped isotope thermometry.

We analyzed calcite fault cements at Courthouse Rock, near Moab, Utah, at the intersection of the through-going southern section of the Moab Fault (fault segment 1, fig. 1) and the northern section, which comprises a series of hard-linked, northwest-trending fault segments (fault segments 2-5, fig. 1; Doelling, 1985, 2002; also known as the Courthouse Fault; Fossen and others, 2005). High-resolution structural mapping by two independent groups has shown that fault segments are constructed from and associated with cataclastic deformation bands, slip surfaces, and joints (Davatzes and others, 2003, 2005; Johansen and others, 2005). Johansen and others (2005) observed two classes of deformation bands at Courthouse Rock: "thick" deformation bands that weather in positive relief, host moderate grain size reduction, and form zones several centimeters wide; and "thin" deformation bands characterized by intense comminution in a bleached zone tenths of millimeters wide. Thin deformation bands and joints are difficult to distinguish at the outcrop. These two styles of fracture, with or without subsequent slip surfaces, are observed to consistently overprint wide zones of "thick" deformation bands (Davatzes and others, 2003, 2005; Johansen and others, 2005), and there is some evidence that joints may also post-date the "thin" deformation bands

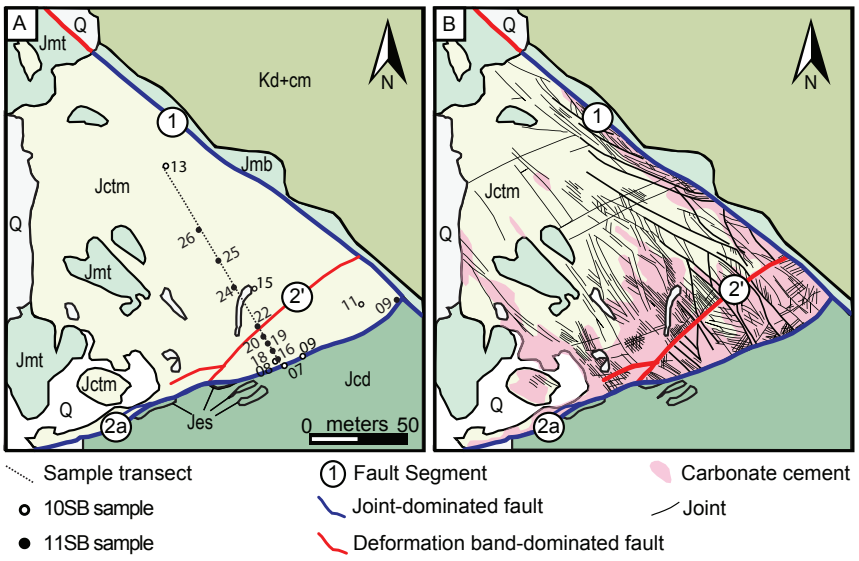

Fig. 2. (A) Geologic map of sampling site B at the intersection of fault segments 1 and 2a (Courthouse Junction), redrawn and simplified from Eichhubl and others (2009). Unit symbols as in figure 1. (A) Sample locations (see table 1). (B) Structural and diagenetic map of sampling site B, with joints as mapped by Davatzes and others (2005) and distribution of calcite cement generalized from Eichhubl and others (2009). See also Johansen and others (2005).

(Johansen and others, 2005). Quartz diagenesis variably reduced the primary porosity of sandstone at Courthouse Rock at early stages of deformation and likely influenced subsequent mechanical behavior of the rock (Johansen and others, 2005). Deformation intensity increases in areas of complex fault geometry, such as at the intersection of fault segments 1 and 2a (Davatzes and others, 2003, 2005; Johansen and others, 2005). At these intersections, fractures are filled with calcite cements, which are found primarily as veins and concretions along fault segment 2a in the Moab Member of the Curtis Formation (formerly mapped as the Moab Member of the Entrada Sandstone), and along fault segment 5 in the Navajo Sandstone (mapping and analysis by Eichhubl and others, 2009). Carbonate cement is absent in areas of the fault characterized by zones of "thick" deformation bands that are not overprinted, suggesting that local fractures occurring at intersections between segments of the Moab Fault acted as preferred fluid conduits (Foxford and others, 1996; Davatzes and others, 2005; Eichhubl and others, 2009).

SAMPLE COLLECTION AND CHARACTERIZATION

We sampled fault-related calcite for clumped isotope thermometry and trace element geochemistry from three sites along and near fault segments near Courthouse Rock (fig. 1). The sampled calcite occurs as veins and associated 2- to 3-cm-thick halos of pore-filling calcite cement surrounding veins (Eichhubl and others, 2009). Site A samples were collected immediately adjacent to fault segment 5 in the Navajo Sandstone (N38°42′25″, W109°44′15″; fig. 1). Site B samples were collected near the intersection of fault segments 1 and 2a along a transect running perpendicular to fault segment 2a and from additional locations in the Moab Member of the Curtis Formation (figs. 1 and 2). Two additional samples were collected at site C (N38°42.5′, W109°44.6′) from the Moab Member of the Curtis Formation in Mill canyon, approxi-

mately 1 km west of Site B, near the intersection of fault segments 2 and 3 (fig. 1; see Davatzes and others, 2005).

Millimeter-to-centimeter length prismatic calcite crystals with abundant fluid inclusions fill cm-to-dm wide joints sampled at site A. In contrast, joints at site B are mm-to-cm wide, filled with mm-to-cm length, flat, white, fibrous calcite crystals. At site C mm-to-cm length, fibrous calcite crystals fill mm-to-cm wide joints. Minor bitumen was found at both sites A and B. Malachite also occurs at sites B and C and is thought to be the most recent cement phase at Courthouse Rock (Eichhubl and others, 2009).

Samples were characterized in thin section with transmitted and polarized light and cold-cathode cathodoluminescence (CL) microscopy, the latter performed using a Technosyn Luminoscope operated at 8–10 kV, 0.5 mA, and 6.7–9.3 Pa to examine the textures of fault cement calcite and to help constrain the origin of diagenetic fluids. Minerals luminesce based on the abundance of trace elements in the crystal lattice, and calcite luminescence, which commonly appears yellow-orange to red, is typically activated by Mn^{2+} ions and quenched by Fe^{2+} ions (Boggs and Krinsley, 2006). At Courthouse Rock, cements within ~500 m of one another display markedly different luminescence patterns and crystal morphologies (figs. 3 and 4). Given the amount of material needed for precise clumped isotope thermometry (~8-12 mg) and trace-element analysis (2-5 mg), some samples contain both vein and halo material, while others contain only vein material (see table 1).

clumped isotope analysis and results

Calcite samples were removed from hand samples by drilling or plucking and powdered with an agate mortar and pestle. For four of the samples, long, prismatic calcite crystals were subdivided into two to three sections parallel to the growth direction prior to powdering to examine possible temperature changes through time (table 1). Previous work indicates no measurable effect on clumped isotope analysis due to these different sampling methods (Swanson and others, 2012).

Clumped isotope samples were pre-treated by soaking in 3 percent H_2O_2 for 45 minutes, followed by rinsing in deionized water and freeze-drying to remove organic material (see table 1 for exceptions). Pre-treating internal lab standards using H_2O_2 does not affect conventional stable isotope or clumped isotope measurements (Tripati and others, 2010). All samples were analyzed at the California Institute of Technology following the methods of Passey and others (2010), described here briefly. CO_2 samples were produced from 8 to 12 mg of calcite reacted in a common acid bath (104% H_3PO_4) at 90 °C for 10 minutes. Product CO_2 was separated from evolved H_2O via passage through multiple cryogenic traps. The CO_2 analyte was then entrained in He carrier gas and passed through a Poropak Q column in a gas chromatograph held at −20 °C. Purified CO_2 was analyzed on a ThermoFinnigan MAT 253 mass spectrometer configured to measure m/z ratios for masses 44 to 49 and screened for mass-48 contaminants. We report Δ_{47} values both in the Caltech reference frame (all Δ_{47} values normalized to stochastic Δ_{47} values and corrected for linearity and scale compression using heated gases; Huntington and others, 2009) and in the absolute reference frame (ARF; Dennis and others, 2011). The transfer function from the Caltech reference frame to the ARF was calculated using a secondary standardization, using assumed Δ_{47} values for 1000 °C heated gases and carbonate standards (Carrara marble, TV-01 calcite, and Carmel calcite; see Appendix A for data and details of transfer function calculations). These Δ_{47} values along with measured $\delta^{13}C$ and $\delta^{18}O$ values (referenced to VPDB) are presented in table 1.

Calcite growth temperature [$T(\Delta_{47})$] was calculated in three ways: (1) using Caltech reference frame Δ_{47} values and the theoretical calcite clumping-temperature equation of Guo and others (2009), which couples a theoretical model of ^{13}C-^{18}O clumping (Schauble and others, 2006) with predicted kinetic isotope effects from

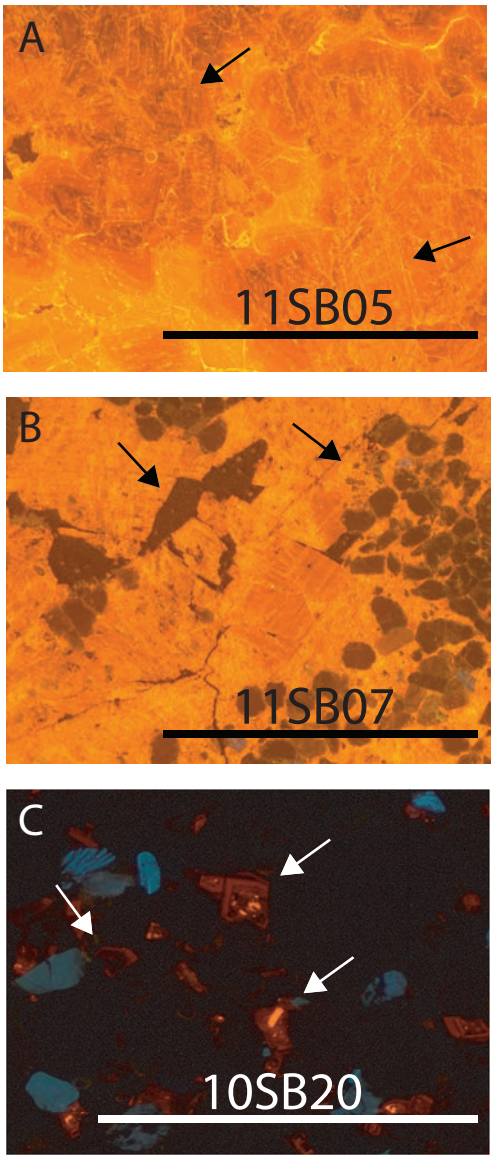

Fig. 3. CL photomicrographs of samples from site A. (A) CL image for sample 11SB05 (91-100 °C), characterized by bright orange luminescence, zoning defined by variations in calcite luminescence and calcite twinning (see arrows); scale bar represents 2 mm. (B) CL image for sample 11SB07 (67-95 °C), characterized by quartz diminution and calcite vein fracture; scale bar represents 2 mm. (C) CL image for sample 10SB20 (128 °C), characterized by zoning defined by variations in calcite luminescence, and extremely bright orange luminescence; scale bar represents 1 mm. See text for further description.

phosphoric acid digestion of carbonate; (2) using ARF Δ_{47} values and the empirical calibration of Ghosh and others (2006) transferred to the ARF by Dennis and others (2011); and (3) using ARF Δ_{47} values and the empirical calibration of Dennis and Schrag (2010) transferred to the ARF by Dennis and others (2011). Temperatures calculated using all three methods are listed in table 1. Although choice of reference

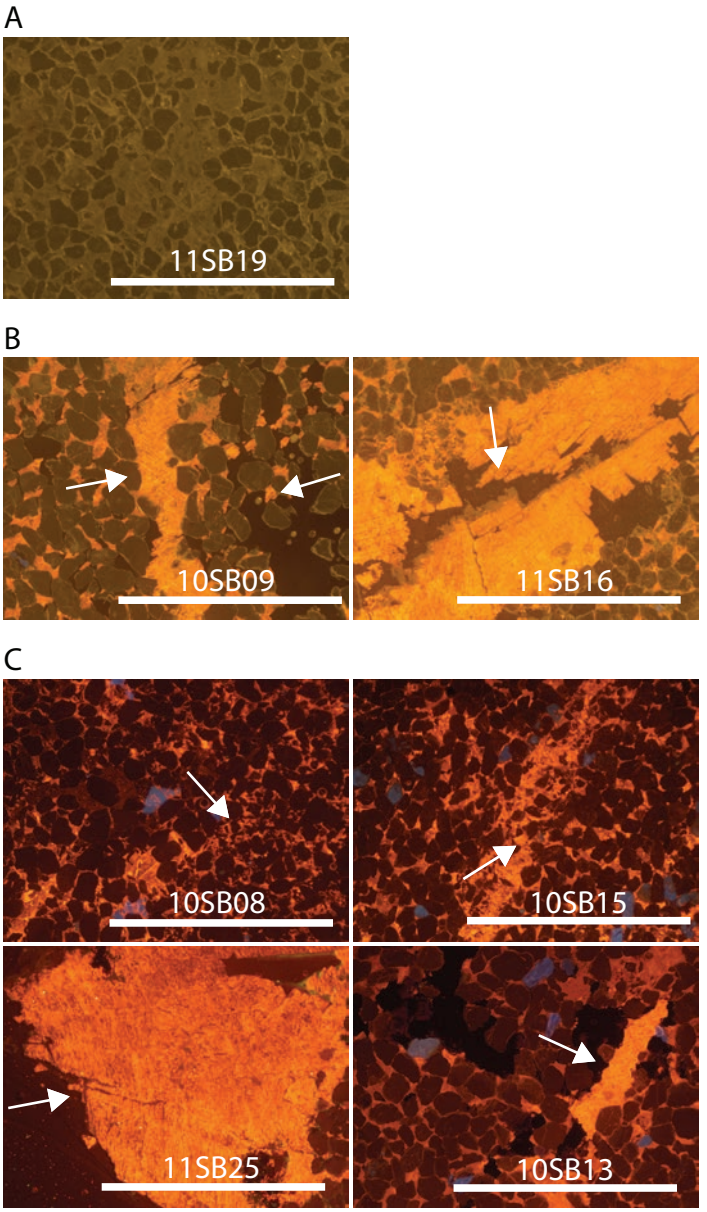

Fig. 4. CL photomicrographs of samples from site B; all scale bars represent 2 mm. (A) CL image for sample 11SB19 (29 °C), characterized by weak to non-luminescent brown calcite cement. (B) CL images for samples 10SB09 (50 °C) and 11SB16 (42 °C), characterized by calcite twinning, calcite vein fracture, and occasional zoning in calcite luminescence, see arrows. (C) CL images for samples 10SB08 (60 °C), 10SB15 (65 °C), 11SB25 (71-73 °C), and 10SB13 (71 °C); characterized by variable orange to orange-red luminescence, calcite twinning, quartz diminution, and zoning in calcite luminescence as described further in the text.

frame and calibration does not significantly impact our interpretations, because the Guo and others (2009) equation has not been transferred to the absolute reference frame and the calibration data of Ghosh and others (2006) extend only from 0 to

TABLE 1

Stable isotopic data for calcite cements

Analysis Date	Sample	Dist. from Fault Seg. 2a (m)	Δ_{47} (‰), Caltech ±1 SE (analytical)	Δ_{47} (‰), ARF[+]	1 SE Δ_{47} (‰) from SD of standards	T(Δ_{47}) (ºC) Caltech, Guo	T(Δ_{47}) (ºC) ARF, Ghosh	T(Δ_{47}) (ºC) ARF, D&S	$\delta^{13}C$ (‰), measured*	$\delta^{18}O_{carb}$ (‰), measured**	$\delta^{18}O_{H2O}$ (‰), calc. (ARF, Ghosh)[#]	$\delta^{18}O_{H2O}$ (‰), calc. (ARF, D&S)[#]
Site A, Navajo Sandstone at Fault Segment 5												
8/22/11	11SB05a	-	0.506 ± 0.004	0.554	0.019	81	64	98	-4.75	-21.5	-12.3	-7.4
8/22/11	11SB05b	-	0.504 ± 0.020	0.552	0.019	82	65	100	-4.74	-20.9	-11.5	-6.6
8/22/11	11SB05c	-	0.516 ± 0.010	0.565	0.019	75	61	91	-4.55	-21.4	-12.7	-8.3
8/25/11	11SB07a-1	-	0.516 ± 0.009									
8/23/11	11SB07a-2	-	0.506 ± 0.008									
-	11SB07a-avg	-	0.511 ± 0.005	0.560	0.013	78	63	95	-5.75	-22.3	-13.2	-8.6
8/26/11	11SB07b-1	-	0.518 ± 0.006									
8/23/11	11SB07b-2	-	0.536 ± 0.010									
-	11SB07b-avg	-	0.524 ± 0.009	0.573	0.013	71	59	86	-6.27	-22.1	-13.7	-9.7
8/25/11	11SB07c	-	0.554 ± 0.010	0.605	0.019	57	50	67	-5.67	-17.6	-10.6	-7.9
9/10/10	10SB20-1[§]	-	0.472 ± 0.009									
9/11/10	10SB20-2[§]	-	0.469 ± 0.008									
-	10SB20-avg[§]	-	0.471 ± 0.002	0.517	0.013	101	76	128	-4.36	-20.6	-9.6	-2.9
Site B, Moab Member of Curtis Formation neaer Courthouse Rock												
9/3/10	10SB07-1		0.558 ± 0.010									
9/10/10	10SB07-2[§]		0.559 ± 0.008									
-	10SB07-avg	0.0	0.559 ± 0.001	0.610	0.013	55	48	64	-3.56	-17.5	-10.9	-8.2
8/31/10	10SB09-1		0.594 ± 0.010									
9/2/10	10SB09-2		0.591 ± 0.010									
9/8/10	10SB09-3[§]		0.573 ± 0.007									
-	10SB09-avg	0.0	0.586 ± 0.007	0.639	0.011	44	41	50	-2.40	-17.1	-11.7	-10.1
8/22/11	11SB09	2.0	0.676 ± 0.007	0.734	0.019	12	20	13	-1.33	-10.9	-9.6	-11.1
8/21/11	11SB16-1		0.609 ± 0.009									
8/26/11	11SB16-2		0.597 ± 0.008									
-	11SB16 -avg	3.0	0.603 ± 0.006	0.657	0.013	37	37	42	-3.10	-18.8	-14.2	-13.2
9/10/10	10SB08-1[§]		0.582 ± 0.010									
9/6/10	10SB08-2[§]		0.553 ± 0.009									
-	10SB08-avg	3.0	0.567 ± 0.020	0.619	0.013	52	46	60	-3.45	-15.6	-9.3	-7.0
8/24/11	11SB18a-1		0.668 ± 0.010									
8/26/11	11SB18a-2		0.671 ± 0.010									
-	11SB18a-avg	8.1	0.669 ± 0.002	0.727	0.013	14	22	15	-0.08	-10.0	-8.3	-9.7

Table 1
(continued)

Analysis Date	Sample	Dist. from Fault Seg. 2a (m)	Δ_{47} (‰), Caltech ±1 SE (analytical)	Δ_{47} (‰), ARF[+]	1 SE Δ_{47} (‰) from SD of standards	T(Δ_{47}) (ºC) Caltech, Guo	T(Δ_{47}) (ºC) ARF, Ghosh	T(Δ_{47}) (ºC) ARF, D&S	$\delta^{13}C$ (‰), measured*	$\delta^{18}O_{carb}$ (‰), measured**	$\delta^{18}O_{H2O}$ (‰), calc. (ARF, Ghosh)[#]	$\delta^{18}O_{H2O}$ (‰), calc. (ARF, D&S)[#]
Site B, Moab Member of Curtis Formation near Courthouse Rock												
8/24/11	11SB18b-1		0.646 ± 0.007									
8/27/11	11SB18b-2		0.673 ± 0.010									
-	11SB18b-avg	8.1	0.657 ± 0.010	0.714	0.013	18	24	20	1.07	-8.5	-6.3	-7.2
8/24/11	11SB18c	8.1	0.665 ± 0.010	0.722	0.019	16	23	17	0.85	-9.1	-7.1	-8.4
8/27/11	11SB19-1		0.642 ± 0.010									
8/21/11	11SB19-2		0.629 ± 0.009									
-	11SB19-avg	12.1	0.634 ± 0.007	0.690	0.013	26	29	29	-1.88	-15.8	-12.7	-12.7
9/5/10	10SB11-1§		0.499 ± 0.009									
9/8/10	10SB11-2§		0.542 ± 0.010									
-	10SB11-avg	15.0	0.520 ± 0.020	0.569	0.013	70	60	88	-3.61	-20.2	-11.6	-7.5
8/27/11	11SB20	17.0	0.628 ± 0.008	0.683	0.019	28	31	31	-0.08	-12.1	-8.6	-8.6
8/28/11	11SB22-1		0.633 ± 0.005									
8/28/11	11SB22-2		0.648 ± 0.003									
-	11SB22-avg	21.8	0.639 ± 0.008	0.695	0.013	24	28	27	0.62	-9.9	-6.9	-7.1
9/3/10	10SB15-1		0.556 ± 0.009									
9/10/10	10SB15-2§		0.560 ± 0.008									
-	10SB15-avg	34.0	0.558 ± 0.002	0.609	0.013	55	49	65	-3.39	-17.6	-10.8	-8.2
8/25/11	11SB24-1		0.518 ± 0.010									
8/26/11	11SB24-2		0.537 ± 0.010									
-	11SB24-avg	45.3	0.527 ± 0.010	0.577	0.013	70	58	84	-2.50	-20.9	-12.6	-8.7
8/24/11	11SB25a	60.3	0.547 ± 0.020	0.598	0.019	60	52	71	-2.68	-20.4	-13.1	-10.1
8/25/11	11SB25b	60.3	0.544 ± 0.009	0.595	0.019	62	53	73	-2.98	-19.6	-12.1	-9.0
8/27/11	11SB26-1		0.592 ± 0.009									
8/21/11	11SB26-2		0.572± 0.010									
-	11SB26-avg	78.8	0.583 ± 0.010	0.636	0.013	45	42	51	-3.41	-19.8	-14.3	-12.7
9/12/10	10SB13-1§		0.534 ± 0.009									
9/9/10	10SB13-2§		0.550 ± 0.010									
-	10SB13-avg	109.0	0.547 ± 0.010	0.598	0.013	60	52	71	-3.34	-18.7	-11.4	-8.4

TABLE 1
(continued)

Analysis Date	Sample	Dist. from Fault Seg. 2a (m)	Δ_{47} (‰), Caltech ±1 SE (analytical)	Δ_{47} (‰), ARF[+]	1 SE Δ_{47} (‰) from SD of standards	T(Δ_{47}) (ºC) Caltech, Guo	T(Δ_{47}) (ºC) ARF, Ghosh	T(Δ_{47}) (ºC) ARF, D&S	$\delta^{13}C$ (‰), measured*	$\delta^{18}O_{carb}$ (‰), measured**	$\delta^{18}O_{H2O}$ (‰), calc. (ARF, Ghosh)[#]	$\delta^{18}O_{H2O}$ (‰), calc. (ARF, D&S)[#]
Site C, Curtis Formation at Mill Canyon												
9/1/10	10SB25-1	-	0.517 ± 0.010									
9/11/10	10SB25-2§	-	0.504 ± 0.010									
9/8/10	10SB25-3§	-	0.511 ± 0.001									
-	10SB25-avg	-	0.511 ± 0.004	0.560	0.011	78	63	95	-4.53	-22.0	-12.9	-8.3
9/11/10	10SB26-1§	-	0.602 ± 0.010									
9/4/10	10SB26-2§	-	0.583 ± 0.009									
-	10SB26-avg	-	0.592 ± 0.009	0.645	0.013	41	40	47	-2.60	-14.6	-9.4	-8.1

Sample names ending in "-1," "-2," or "-3" are replicate analyses of the same powder; sample names ending in "-average" represent the weighted mean of replicate analyses of the same sample. Samples starting with "10" include vein and halo calcite; samples starting with "11" contain only vein calcite. Sample names with a, b, and c indicate samples representing different stages of growth in the same crystal, with "a" predating "b" and "b" predating "c."

Δ_{47} values denoted "Caltech" are presented in Caltech reference frame, while Δ_{47} values denoted "ARF" are presented in absolute reference frame of Dennis and others (2011); Δ_{47} value in ARF = 1.0567 (Δ_{47}, Caltech) + 0.0197 ($R^2 > 0.99$), following methods of Dennis and others (2011), as shown in Data Repository. T(Δ_{47}) values denoted "Caltech, Guo" are calculated from Δ_{47} values in Caltech reference frame using the theoretical equation of Guo and others (2009), for calcite. T(Δ_{47}) values denoted "ARF, Ghosh," and "ARF, D&S" are calculated from Δ_{47} values in the absolute reference frame, and calibration equations of Ghosh and others (2006) and Dennis and Schrag (2010), respectively, each converted to the absolute reference frame as in Dennis and others (2011).

* Values are referenced to VPDB; average ±0.06‰ (1 SE) for externally replicated samples.

** Values are referenced to VPDB; average ±0.1‰ (1 SE) for externally replicated samples.

[#] Values are referenced to VSMOW. Values are calculated from measured $\delta^{18}O_{carb}$ and T(Δ_{47}) using the equation of Kim and O'Neil (1997) for calcite.

[§] 2010 sample was pre-treated in H_2O_2 solution (see text for details). Not all samples processed in 2010 were pre-treated. All samples processed in 2011 were pre-treated.

TABLE 2
ICP-OES results

Sample	Ba/Ca (ppb)	Sr/Ca (ppb)	Ba (ppb)	Sr (ppb)	Ca (ppm)
Site A, Navajo Sandstone at fault segment5					
11SB07	<0.1	1.7	<0.1	33.7	20.0
11SB05	<0.1	2.5	<0.1	77.4	31.4
Site B, Moab Member of Curtis Formation at Courthouse Rock					
11SB09	0.1	0.6	2.1	10.9	17.1
11SB16	<0.1	1.0	<0.1	8.8	9.1
11SB19	<0.1	0.8	<0.1	4.8	6.1
11SB24	<0.1	1.3	0.1	33.0	25.1
11SB25	<0.1	0.8	2.0	20.5	24.1
11SB26	0.1	0.9	2.3	16.3	17.9

50 °C, we limit our discussion in the text to calcite temperatures calculated using method (3; "ARF, D&S"). We calculated $\delta^{18}O_{H_2O}$ values (referenced to VSMOW) from $T(\Delta_{47})$ and measured $\delta^{18}O_{carb}$ using the calcite-water fractionation factor of Kim and O'Neil (1997). We discuss $\delta^{18}O_{H_2O}$ values derived from $T(\Delta_{47})$ (ARF, D&S) in the text and figures, and we provide $\delta^{18}O_{H_2O}$ values derived from $T(\Delta_{47})$ (ARF, Ghosh) in table 1 for reference; note that $\delta^{18}O_{H_2O}$ values derived from $T(\Delta_{47})$ (Caltech, Guo) fall between these values.

Samples were analyzed one to three times, with average values of Δ_{47} ranging from 0.517 to 0.734 permil (ARF) and $T(\Delta_{47})$ values corresponding to calcite growth temperatures of 13 to 128 °C (ARF, D&S). The Δ_{47} values for samples representing different stages of growth in the same crystal (indicated with a, b, c in sample name, where "c" represents later growth; table 1) agree within analytical error (1 SE) for samples 11SB05, 11SB18, and 11SB25 (average temperatures of 96 ± 5 °C, 17 ± 2 °C, and 72 ± 1 °C (1 SD), respectively). While Δ_{47} values for samples 11SB07a and 11SB07b are within 1 SE (average temperature 90 ± 6 °C, 1 SD); the Δ_{47} value for 11SB07c is >1 SE higher, corresponding to a temperature of 67 °C. Sample average values for $\delta^{18}O_{carb}$ range from −22.3 to −8.5 permil, and values for $\delta^{13}C$ range from −6.27 to 1.07 permil, with average precisions for externally replicated samples of ±0.1 permil and ±0.06 permil, respectively (1 SE). Calculated $\delta^{18}O_{H_2O}$ values range from −13.2 to −2.9 permil (table 1).

TRACE ELEMENT ANALYSIS AND RESULTS

A subset of the calcite samples from sites A and B was prepared for trace element analysis via inductively coupled argon plasma optical emission spectroscopy (ICP-OES) at the University of Washington. Powdered calcite in 2 to 5 mg aliquots was reacted in 3 mL of nitric acid for 10 minutes to dissolve the solid $CaCO_3$. Each $CaCO_3$—HNO_3 solution was then diluted by volume to 50 mL and analyzed on a Perkin-Elmer 3300DV. ICP-OES trace element analyses were performed in an attempt to further constrain variability in the origin of the fluids from which samples at and within sites A and B precipitated; the results show only minor variation in Ba/Ca and Sr/Ca ratios among samples from sites A and B, with most measured values being below the detection limit of 0.1 ppb (table 2).

DISCUSSION

Our $T(\Delta_{47})$ results confirm previous observations that carbonate cements along the Moab Fault precipitated from multiple fluids (Chan and others, 2000; Eichhubl

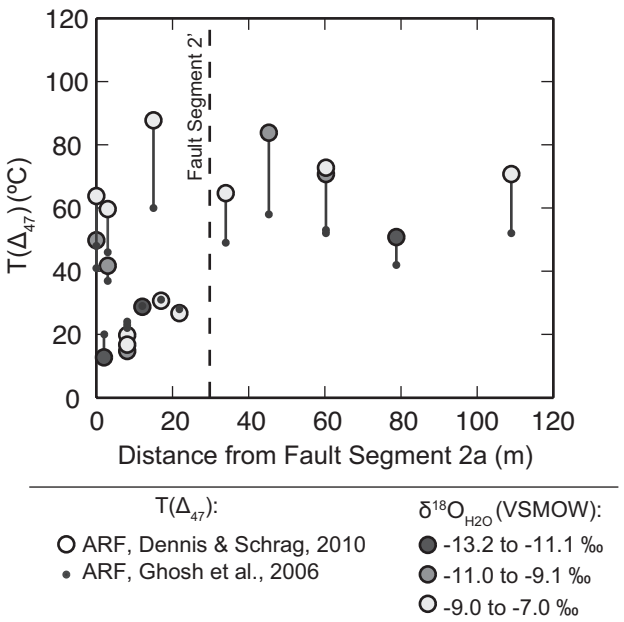

Fig. 5. Distance along the sample transect north of fault segment 2a versus $T(\Delta_{47})$ for samples from site B. Symbol shading indicates the oxygen isotopic composition of the fluid from which the cement precipitated ($\delta^{18}O_{H_2O}$, VSMOW‰, ARF, D&S). Large circles indicate $T(\Delta_{47})$ calculated from Δ_{47} values in the absolute reference frame and temperature calibration of Dennis and Schrag (2010), as discussed in text. Small gray circles connected to these large circles indicate $T(\Delta_{47})$ for the same sample calculated from Δ_{47} values in the absolute reference frame and temperature calibration of Ghosh and others (2006), for reference.

and others, 2009), and provide new evidence that cement growth occurred over a wide range of temperatures that varied spatially at the meter-scale. Although for simplicity the following sections present calcite temperatures calculated using the absolute reference frame and Dennis and Schrag (2010) calibration, our conclusions are insensitive to the choice of reference frame or calibration (table 1; figs. 5-7).

Constraints on Fluid Flow and Cementation at Site A

Based on previous stable isotopic analyses, fluid inclusion work, and basin history models, we anticipated that cements associated with fault segment 5 (site A; fig. 1) precipitated from volumetrically minor basinal fluids mixing with meteoric water, during or closely following maximum burial of the Moab Member following mid-Cenozoic faulting (Nuccio and Condon, 1996; Chan and others, 2000; Garden and others, 2001; Eichhubl and others, 2009). Therefore, we expected cement temperatures and isotopic compositions at site A to reflect calcite precipitation from meteoric waters at temperatures near those of the host rock (Navajo Sandstone) at maximum burial depth of ~2 km (~80-100 °C; Nuccio and Condon, 1996; Vrolijk and van der Pluijm, 1999; Garden and others, 2001).

Our $T(\Delta_{47})$ data from site A are consistent with this hypothesis, clustering around 70 to 100 °C for vein calcite samples (11SB05a, b, c and 11SB07a, b, c) and ranging up to 128 °C for one sample (10SB20) containing both vein and halo calcite. Calcite in sample 10SB20 occurs as pore-filling cement that exhibits zoning defined by variations in luminescence, which suggests growth over an extended period of time with changing fluid trace element composition (fig. 3C). Calcite zones in this sample are

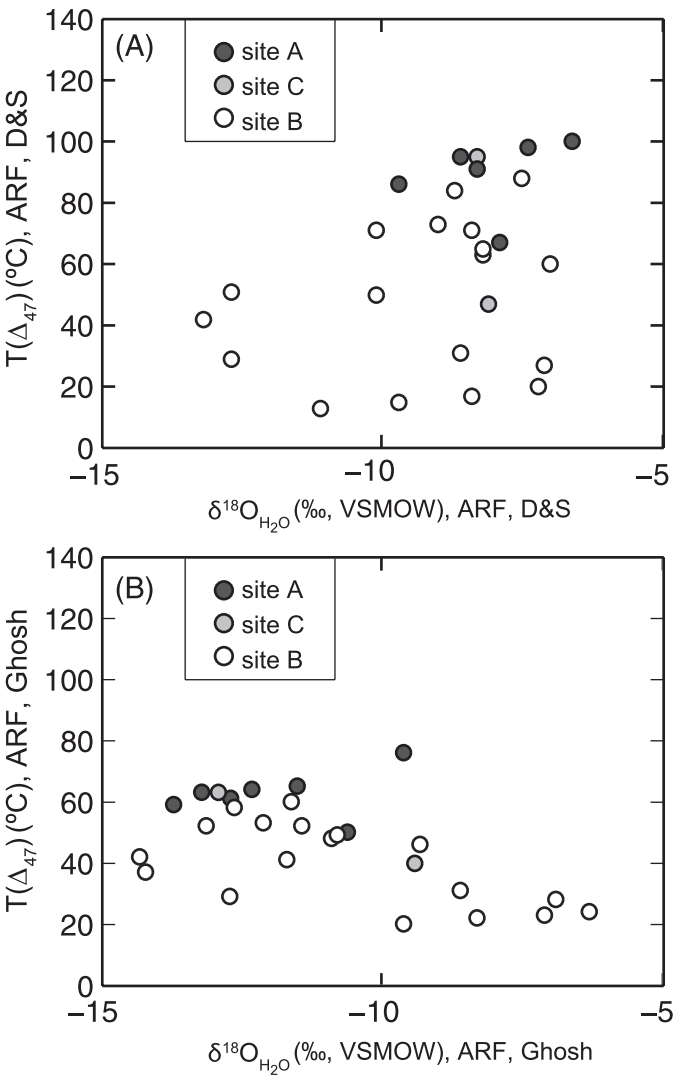

Fig. 6. Calculated $\delta^{18}O_{H_2O}$ versus $T(\Delta_{47})$ values for all samples at sites A, B, and C. Error bars are smaller than symbol size. There is no correlation between fluid isotopic composition and calcite precipitation temperature, indicating diagenetic cements precipitated from fluids with a range of oxygen isotopic compositions over a wide range of temperatures as discussed in the text. (A) $T(\Delta_{47})$ and $\delta^{18}O_{H_2O}$ values calculated from Δ_{47} values in the absolute reference frame and the temperature calibration of Dennis and Schrag (2010). (B) $T(\Delta_{47})$ and $\delta^{18}O_{H_2O}$ values calculated from Δ_{47} values in the Caltech reference frame and the temperature calibration of Ghosh and others (2006).

commonly bright orange, red, or dark red luminescent to non-luminescent, and where bright orange luminescent cement is present, it is commonly the earliest phase of growth at the center of calcite crystals (fig. 3C). Sample 10SB20 also contains bitumen, suggesting that the cement precipitated from a fluid that interacted with hydrocarbons. For the cooler samples, sample 11SB05 shows zoning in calcite crystals defined by bright orange to yellow luminescence, as well as pervasive calcite twinning (fig. 3A). Sample 11SB07 shows the same bright orange to yellow luminescence as 11SB05, but it

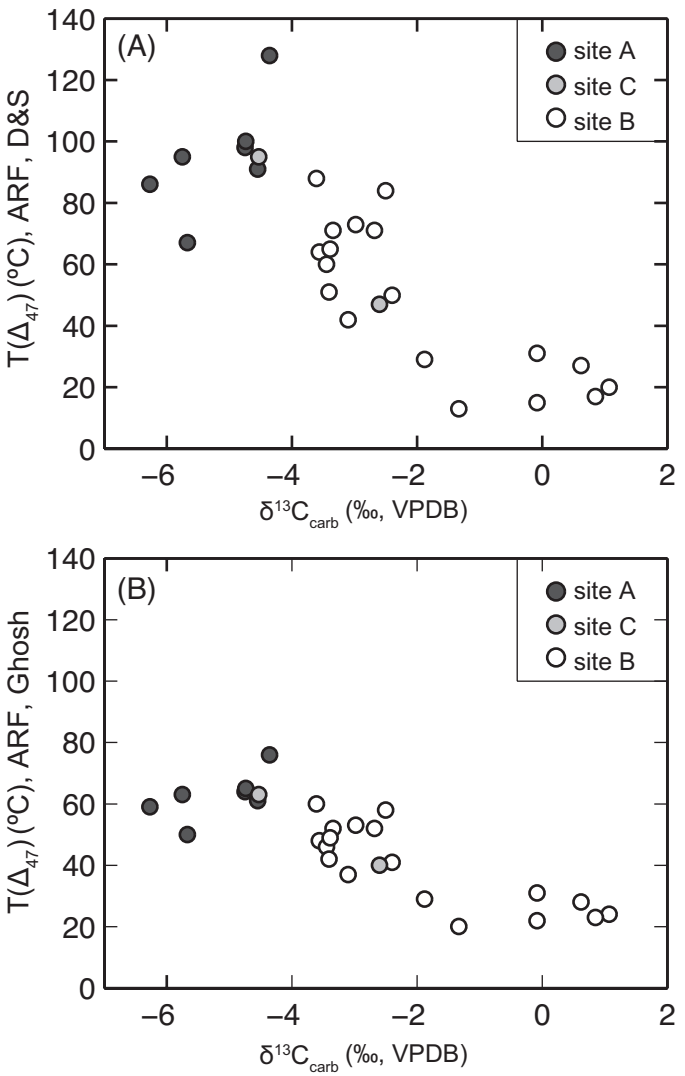

Fig. 7. Measured $\delta^{13}C$ versus $T(\Delta_{47})$ values for all samples at sites A, B, and C. Error bars for $\delta^{13}C$ are smaller than symbol size. Cement temperature and carbon isotopic composition are correlated at site B (r^2 = 0.65) and across the study area (r^2 = 0.67), indicating changes in the carbon pool with changing calcite precipitation temperature, and therefore changing diagenetic fluid source. (A) $T(\Delta_{47})$ calculated from Δ_{47} values in the absolute reference frame and the temperature calibration of Dennis and Schrag (2010). (B) $T(\Delta_{47})$ calculated from Δ_{47} values in the Caltech reference frame and the temperature calibration of Ghosh and others (2006).

exhibits only minor zoning defined by variations in calcite luminescence and calcite twinning (fig. 3B). Although all samples from site A precipitated at elevated temperatures, the variability in $T(\Delta_{47})$ and in calcite luminescence at site A suggest that different temperature calcites precipitated from different fluid sources at different times.

The range of observed fluid inclusion homogenization temperatures (T_H = 84-125 °C) for the calcite sample from site A analyzed by Eichhubl and others (2009)

overlaps with the range of clumped isotope temperatures. Eichhubl and others (2009) suggest that cements with temperatures greater than ~100 °C likely precipitated from minor pulses of hot basinal fluids ascending the Moab Fault. Sample 10SB20 (128 °C), which exhibits a distinctive luminescence pattern (fig. 3C), may represent precipitation from one such pulse of hot basinal fluids.

The oxygen and carbon isotopic compositions of calcite cements from site A are also consistent with the hypothesis that the cements precipitated from deeply circulating meteoric waters. Calculated $\delta^{18}O_{H_2O}$ values for waters in equilibrium with site A cements range from −10 to −3 permil, enriched in ^{18}O with respect to modern meteoric waters in the Paradox Basin (−15 to −12‰ VSMOW; Spangler and others, 1996) (table 1). This enrichment in ^{18}O could be attributed to a variety of factors including climate change, evaporative enrichment at the surface, or subsurface interactions between waters and host rocks. Carbon isotopic values for site A vein calcites (−6.3 to −4.4‰) are slightly depleted in ^{13}C relative to local limestones (+1 to −4‰ VPDB; Garden and others, 2001), but significantly more enriched in ^{13}C than methanogenic carbonates (−30 to −40‰ VPDB; Boles and others, 2004; Eichhubl and others, 2009). The intermediate carbon compositions at site A and association of bitumen with calcite veins observed by us and previous workers at fault segment 5 (Eichhubl and others, 2009) indicate that calcite cements precipitated from fluids that scavenged bicarbonate from local limestones, groundwater, and residual hydrocarbons.

Constraints on Fluid Flow and Cementation at Site B

Site B (Courthouse Rock) is located 500 m northwest of site A, where the structural architecture is defined by both deformation bands and intense secondary fracturing at a fault intersection (Davatzes and others, 2005; Johansen and others, 2005). The site is divided grossly into two domains by a second-order, deformation-band fault (labeled 2′ in fig. 2).

Our new carbon and oxygen isotopic data from site B within 30 m of fault segment 2a are consistent with previously published isotopic data that suggest a dominantly meteoric source for fluids from which the cements precipitated; however, the $\delta^{18}O$ and $\delta^{13}C$ values of calcite we collected on a transect perpendicular to the fault segment suggest systematic spatial variations in diagenetic fluid sources and calcite cementation. While both our calcite $\delta^{13}C$ data and the data of Eichhubl and others (2009) range from −3.5 to +1.3 permil VPDB between fault segments 2a and 2′, our new data for cements north of fault segment 2′ all plot near 3 permil, suggesting a change in the carbon pool from which the cements were sourced (fig. 8). In addition, our data indicate calcite $\delta^{18}O$ and $\delta^{13}C$ values are correlated, with $\delta^{18}O_{carb}$ values varying from −19 to −9 permil VPDB between fault segments 2a and 2′ and clustering around −19 permil north of segment 2′ (fig. 9), suggesting spatial heterogeneity of diagenetic fluid sources and calcite cementation.

The $T(\Delta_{47})$ data show that the temperature of the diagenetic fluids from which calcite cements grew also varied considerably over distances of tens of meters (fig. 5). Clumped isotope temperatures for cement samples collected north of fault segment 2′ range from 51 to 84 °C, overlapping the range of temperatures observed at site A. However, cements in the zone of abundant fracturing between fault segments 2 and 2′ range from 13 to 88 °C. The lowest temperatures in this range are too cool to record calcite precipitation from fluids thermally equilibrated with the host rock near maximum burial of the host sandstone, further suggesting multiple fluid sources.

Constraints on Fluid Flow and Cementation at Site C

Site C is located at the intersection of fault segments 2b, 2c and 3 (mapped by Davatzes and others, 2005; Eichhubl and others, 2009) and is characterized by both

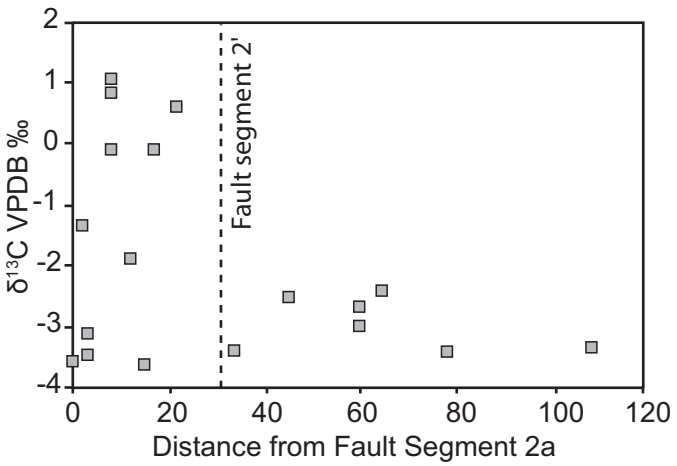

Fig. 8. Distance along the sample transect north of fault segment 2a versus $\delta^{13}C$ for samples from site B. The greatest variation in carbon composition occurs in the heavily jointed region between fault segments 2a and 2′ (0-30 m on the figure, see fig. 2B). Analytical uncertainty (1 SE) in $\delta^{13}C$ and distance is smaller than the symbol size.

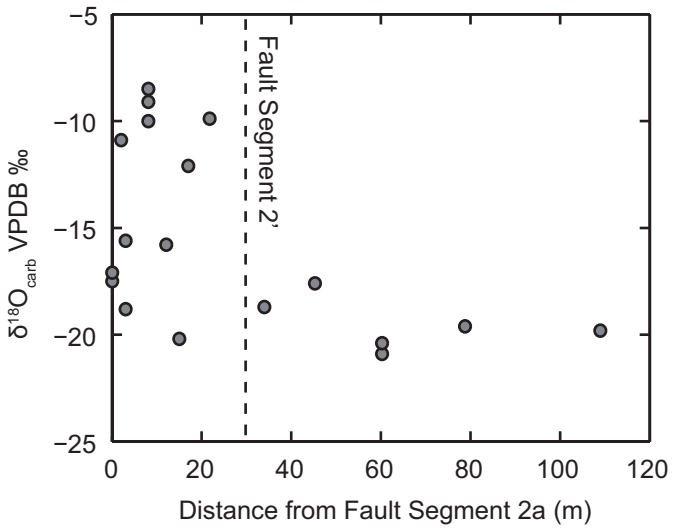

Fig. 9. Distance along the sample transect north of fault segment 2a versus $\delta^{18}O_{carb}$ for samples from site B. Analytical uncertainty is smaller than the symbol size. The greatest variation in the oxygen isotopic composition of calcite cements occurs in the heavily jointed region between fault segments 2a and 2′. Based on $\delta^{18}O_{carb}$ data alone it is not possible to determine if the variation reflects variation in fluid temperature, isotopic composition, or both.

joints and deformation bands. We present $T(\Delta_{47})$ data for two cement samples from site C. The first sample at site C yields a $T(\Delta_{47})$ value of 95 °C; this result is similar to average temperatures at site A and the highest temperatures at site B, and is consistent with estimated temperatures of the country rock during maximum burial. The second sample at this site yields a $T(\Delta_{47})$ value of 47 °C, which is within the range of

temperatures observed for cements collected within 30 m of fault segment 2 at site B, and is significantly cooler than expected for fluids ascending the fault or in the adjacent host rock following deformation near maximum burial. These samples plot on the $\delta^{13}C$ versus $T(\Delta_{47})$ trend defined by the site A and B samples (fig. 7).

Hypotheses for the Origin of Low-Temperature Cements

While warm cement temperatures can be explained by a fluid-cementation regime described by meteoric groundwaters at ambient geothermal temperatures interacting with a deeper basin source (for example, Chan and others, 2000; Eichhubl and others, 2009), a fundamentally different regime varying in time and/or space must be invoked to explain how some carbonate cements formed at temperatures consistent with Earth-surface conditions. We propose two end-member scenarios that could explain precipitation of the low-temperature cements at sites B and C: the cements could have grown from either 1) fluids traveling through fractures from the surface to depth sufficiently rapidly that calcite precipitated before the fluids thermally equilibrated with the host rock, or 2) fluids thermally equilibrated with the host rock when it was near the surface.

Scenario 1 invokes highly conductive joints to enable rapid downward migration of surficial fluids and low-temperature cement growth at depth. This hypothesis predicts that the coolest cements precipitate at fault intersections where fracture density is observed to be greatest (Davatzes and others, 2005; Johansen and others, 2005; Eichhubl and others, 2009), and the greatest quantity of surface water might be expected to rapidly infiltrate the fault. Cements farther from the main fault segments might record warmer temperatures, reflecting the warming of surface fluids as they migrated away from this conduit through the warm host sandstone at depth. Thus, this scenario predicts that the spatial distribution of cool cements is limited to regions of fracturing adjacent to faults. Migration of cool surficial fluids away from the fault would be inhibited by low permeability zones of deformation-band faults and associated slip surfaces. Scenario 1 does not predict relative timing of cool and warm cements.

Scenario 2 proposes that the cool clumped isotope temperatures represent calcite growth near the Earth's surface, late in the exhumation history of the Basin. This scenario predicts the relative ages of warm and cool carbonate cements: early calcite precipitated at elevated temperatures from upward migrating fluids, while later cements precipitated throughout exhumation of the host sandstone. Scenario 2 does not require cool cements to be restricted to near-fault fractures.

In both scenarios, we expect cements with meteoric water signatures, although higher-temperature calcite samples might be enriched in ^{18}O and depleted in ^{13}C due to interaction with silicate rocks and residual hydrocarbons at depth. At all three sites, calculated values of $\delta^{18}O_{H_2O}$ in equilibrium with the calcites suggest a dominantly meteoric source with variable contribution from basinal waters enriched in ^{18}O. Although $\delta^{18}O_{H_2O}$ values and $T(\Delta_{47})$ are not strongly correlated (fig. 6) and thus do not provide insight in to the source(s) of warm versus cooler fluids, calcite $\delta^{13}C$ values at site B vary with distance from fault segment 2a and are highly correlated with $T(\Delta_{47})$ ($R^2 = 0.65$), indicating that the cooler cements reflect a carbon source more enriched in ^{13}C ($\delta^{13}C$ approximately -2 to 1‰) than the warmer cements ($\delta^{13}C$ approximately -4 to -3‰). These warmer cements approach the carbon isotopic compositions for calcites at site A, which we infer to have precipitated from fluids migrating upward along the fault as previously suggested by Eichhubl and others (2009).

Systematic variability in calcite luminescence observed at site B also supports the notion that the different temperature cements precipitated from multiple fluid sources (fig. 4). Calcite cement in sample 11SB19, which precipitated at low temperature (29 °C), is non-luminescent to weakly luminescent brownish orange and lacks

twinning or zoning (fig. 4A). In contrast, the higher temperature samples (between 42 and 50 °C) we examined show orange to bright orange luminescence, extensive calcite twinning, occasional zoning, and fractured calcite crystals within veins (fig. 4B). Although the luminescence of the warmer (60-73 °C) cements at site B is variable, showing weak to bright luminescence in orange, reddish-orange and yellow (fig. 4C), these cements commonly exhibit luminescence that is darker in color (more reddish-orange than yellow-orange) compared to the 42 to 50 °C cements. Zoning defined by variations in calcite luminescence, calcite twinning, and occasional quartz diminution characterize the high temperature samples.

To evaluate the relative timing of warm versus cool cements, we measured $T(\Delta_{47})$ variation within single calcite crystals. If the cool cements grew exclusively from cool, shallow groundwaters following significant exhumation of the host sandstone (scenario 2), we expect cement temperatures to decrease with time. Three sub-sampled calcite crystals from sites A and B have Δ_{47} values for different aliquots of the same crystal that agree within 1 SE, and therefore these samples do not show significant cooling through time (11SB05a,b,c; 11SB18a,b,c and 11SB25a,c; table 1). For sample 11SB07 from site A, Δ_{47} values for subsamples a and b show no variation in temperature, and although the Δ_{47} value for subsample c is more than 1 SE higher than the other aliquots of calcite taken from the same crystal, the Δ_{47} values for all subsamples of 11SB07 agree within 2 SE. Thus the data do not support significant cooling of the fluid during crystal growth and are not cool enough to represent Earth-surface temperatures. However, since the timing of crystal growth is unknown, the absence of cooling during crystal growth does not rule out near-surface cement growth from cool groundwater. No other samples provide constraints on the relative timing of low- and high-temperature cements.

The fault-normal transect at site B illustrates the spatial variability in the temperature of carbonate cements (fig. 5). While the warmest (64-88 °C) cements are found associated with veins and concretions at distances of 3 to 109 m from fault segment 2a, cool (13-27 °C) carbonate cements are limited to the highly-fractured region between fault segments 2a and 2′ (fig. 2). The variability in $\delta^{18}O_{H_2O}$ and $\delta^{13}C$ values is similarly reduced across segment 2′ (figs. 8 and 9). This pattern suggests that deformation band-dominated fault segment 2′ may have acted as a baffle against lateral flow of low-temperature fluids, arguing for rapid penetration of surface waters flowing down the high-permeability zone around 2a (scenario 1). If cool fluids infiltrated the host rock only following significant exhumation when the host sandstone was near the surface (scenario 2), low-temperature calcite would be expected throughout given the presence of fractures on either side of 2′ (fig. 2). Similar to site B, site C, which also hosts both cool and warm cements, is a structurally complex fault interaction zone (Davatzes and others, 2005), further supporting the inference that secondary fracturing controls the spatial distribution of cool cements.

Is it reasonable to infer that cold surface waters could reach depths of 2 km without warming? We can address this problem by evaluating the thermal Peclet number (Pe), a dimensionless value that represents the contribution of advective versus conductive heating. Following Ingebritsen and others (2006): $Pe = q_w c_w \rho_w L / K_{rock}$; where q_w, c_w, and ρ_w are the flow rate, heat capacity, and density of the fluid, K_{rock} is the thermal conductivity of the host rock and L is a characteristic length scale. When $Pe < 1$, conduction dominates and fluid temperature is equilibrated with the rock; when $Pe > 5$, the system is essential isothermal, dominated by advection, and controlled by the source-fluid temperature. Over a length scale of 10 km, assuming fixed temperature boundaries, a standard geothermal gradient (25 °C/km), standard physical properties for water and rock (c_w = 4.2 kJ/kg/°C; $\rho_w = 10^3$ kg/m^3; K_{rock} = 2 W/m/°C), cool water can reach 2 km depth at moderate flow rates of $>10^{-10}$ m/s.

These values give a Peclet number of 2, of the same order as observations from hydrological experiments in fracture-dominated flow (Anderson, 2005, and references therein).

Based on our observations from calcite cements at sites A, B, and C, it appears that interaction of meteoric groundwater and a deeper basinal source led to calcite cementation throughout the study area, while down-going surface waters penetrated rapidly to significant depth only at fault intersection zones where fracture density is greater. These clumped isotope data provide new insight into fluid sources and pathways controlled by structural complexity, and combined with carbon and oxygen isotopic data, CL microscopy, and other observations of previous workers are consistent with findings that the structural architecture influences fluid flow and cementation in this area (Eichhubl and others, 2009).

CONCLUSIONS

Clumped isotope thermometry along the Moab Fault at Courthouse Rock show that calcite veins precipitated from meteoric waters over a wide range of temperatures (13-128 °C). Our work provides evidence for carbonate growth from Earth surface-temperature fluids along the Moab Fault and suggests that the Fault served as a conduit for both ascending and descending fluids. This study area is characterized by fault zone heterogeneity, with faults formed from both deformation bands and joints. Our results support earlier findings that interactions between these two classes of structures determined where fluids migrated at Courthouse Rock. The spatial distribution of low-temperature cements argues for rapid penetration of surface waters flowing down intensely-fractured fault intersections, and suggests that deformation-band faults served as low-permeability baffles, preventing lateral migration of cold fluids. Thus, it appears that structural heterogeneity is responsible for cement precipitation over a wide range of temperatures prior to exhumation of the host rock. Carbonate clumped isotope thermometry quantified calcite growth temperatures below ~30 °C and the spatial pattern of cement temperatures, and it is only these new data that made our interpretation possible. Our study suggests this new technique permits evaluation of the role of these important structures in influencing fluid flow in ancient fault systems.

ACKNOWLEDGMENTS

Acknowledgment is made to the donors of the American Chemical Society Petroleum Research Fund for support of this research (ACS-PRF grant 49709 and NSF grant EAR-115613 to KWH). We thank the donors of the University of Washington, Department of Earth and Space Sciences for support of this research (George Goodspeed Fellowship and Dorothy G. Stephens Fellowship to SCB). We thank John Eiler, Nami Kitchen and Ron Sletten for generous laboratory access and assistance. We thank Gerd Winterleitner and David Birlenbach for field assistance, and Winterleitner, David Budd and Peter Eichhubl for discussions that guided our thinking on this project. This manuscript benefitted from thoughtful reviews by Haakon Fossen, Peter Eichhubl and an anonymous reviewer.

APPENDIX A

SECONDARY STANDARDIZATION TO "ABSOLUTE REFERENCE FRAME"

The clumped isotope samples in this study were analyzed along with heated gases and carbonate standards in two analytical sessions (analytical sessions 1 and 2), and we report all of the Δ_{47} values both in the Caltech reference frame and in the "absolute reference frame" described by Dennis and others (2011). The Δ_{47} values reported in the Caltech reference frame were normalized to stochastic Δ_{47} values and corrected for linearity and scale compression using CO_2 gases heated to 1000 °C (Huntington and others, 2009), and the heated gas data used for these normalizations are reported in table A1. The transfer function from the Caltech reference frame to the absolute reference frame was calculated using a secondary

TABLE A1

Isotopic results for heated gases

date	$\delta^{13}C$ (PDB)	$\delta^{13}C$ stdev	$\delta^{18}O$ gas (SMOW)	$\delta^{18}O$ stdev	δ_{47} (v. Oz)	δ_{47} stdev	Δ_{47} (v. Oz)	Δ_{47} stdev	Δ_{47} sterror	δ_{48} (v. Oz)	Δ_{48} (v. Oz)	Δ_{48} stdev
Analytical Session 1, 8/31/2010-9/11/2010:				*best-fit heated gas line:*	$_{47} = 0.0106 (\delta_{47}) - 0.8181 (R^2 = 0.97)$							
9/1/10	-11.170	0.003	28.750	0.008	-4.467	0.017	-0.885	0.024	0.009	8.815	1.496	0.191
9/2/10	-10.704	0.003	59.522	0.009	26.752	0.014	-0.506	0.036	0.013	86.235	16.686	0.913
9/3/10	-12.356	0.003	25.753	0.003	-8.563	0.022	-0.878	0.040	0.014	2.081	0.630	0.329
9/4/10	-10.679	0.003	58.629	0.003	25.855	0.028	-0.543	0.017	0.006	84.441	16.719	0.879
9/5/10	-10.191	0.005	58.122	0.002	25.827	0.013	-0.557	0.018	0.006	82.674	16.031	0.946
9/6/10	-10.356	0.002	29.696	0.003	-2.693	0.020	-0.833	0.026	0.009	12.064	2.874	0.260
9/7/10	-10.798	0.004	57.999	0.007	25.088	0.019	-0.569	0.040	0.014	81.572	15.236	2.233
9/8/10	-10.588	0.003	29.311	0.017	-3.379	0.012	-0.914	0.073	0.026	10.890	2.461	0.245
9/9/10	-10.640	0.001	29.950	0.002	-2.743	0.020	-0.859	0.021	0.001	12.445	2.757	0.235
9/10/10	-10.546	0.001	28.841	0.004	-3.703	0.020	-0.815	0.021	0.007	9.526	2.021	0.413
9/11/10	-11.043	0.003	28.979	0.003	-4.092	0.013	-0.858	0.034	0.012	10.095	2.321	0.318
Analytical Session 2, 8/21/2011-8/28/2011:				*best-fit heated gas line:*	$_{47} = 0.0075 (\delta_{47}) - 0.7774 (R^2 = 0.99)$							
8/20/11	-10.669	0.005	60.631	0.005	27.822	0.014	-0.565	0.032	0.011	83.293	11.816	0.180
8/20/11	-10.583	0.004	29.047	0.004	-3.521	0.018	-0.800	0.024	0.008	8.878	0.979	0.193
8/20/11	-10.629	0.004	61.120	0.009	28.353	0.024	-0.557	0.020	0.007	84.459	11.972	0.165
8/21/11	-10.640	0.002	27.928	0.008	-4.673	0.018	-0.793	0.014	0.005	6.311	0.604	0.178
8/23/11	-10.689	0.002	58.061	0.013	25.239	0.025	-0.588	0.021	0.008	77.451	11.249	0.161
8/24/11	-10.625	0.006	29.247	0.013	-3.357	0.030	-0.793	0.037	0.013	9.551	1.256	0.123
8/25/11	-10.681	0.004	58.438	0.023	25.623	0.047	-0.585	0.033	0.012	78.485	11.499	0.147
8/27/11	-10.517	0.007	29.532	0.033	-2.989	0.073	-0.811	0.038	0.013	10.281	1.427	0.203
8/28/11	-10.654	0.004	57.958	0.015	25.174	0.062	-0.586	0.026	0.009	77.554	11.542	0.186
8/29/11	-10.395	0.002	29.305	0.002	-3.091	0.018	-0.809	0.018	0.006	9.657	1.248	0.235
8/30/11	-10.606	0.007	58.404	0.016	25.659	0.025	-0.581	0.017	0.006	78.302	11.372	0.191
8/31/11	-10.651	0.003	29.126	0.004	-3.512	0.028	-0.794	0.032	0.011	9.204	1.130	0.166
9/1/11	-11.007	0.002	56.924	0.004	23.788	0.030	-0.589	0.030	0.011	74.960	11.061	0.238
9/2/11	-10.881	0.003	28.676	0.004	-4.195	0.028	-0.810	0.031	0.011	8.204	1.012	0.194
9/2/11	-10.433	0.003	57.917	0.013	25.310	0.033	-0.620	0.031	0.011	77.397	11.452	0.185
9/4/11	-10.784	0.004	57.019	0.004	24.094	0.025	-0.600	0.025	0.009	75.326	11.224	0.225
9/6/11	-10.984	0.002	28.195	0.007	-4.763	0.015	-0.804	0.029	0.010	7.209	0.960	0.156
9/7/11	-10.879	0.003	56.047	0.008	23.032	0.014	-0.606	0.028	0.010	73.204	11.085	0.186
9/8/11	-10.306	0.005	30.202	0.003	-2.137	0.013	-0.816	0.030	0.011	11.816	1.624	0.167
9/9/11	-10.474	0.003	56.175	0.010	23.570	0.016	-0.599	0.023	0.008	74.126	11.707	0.140
9/10/11	-10.614	0.004	29.629	0.006	-3.000	0.020	-0.814	0.038	0.014	10.601	1.536	0.281
9/11/11	-10.641	0.003	55.756	0.005	23.000	0.028	-0.588	0.029	0.010	72.879	11.336	0.190

All values are reported in ‰. "Oz" refers to working reference gas by Oztech.

Table A2

Isotopic results for carbonate standards

date	$\delta^{13}C$ (PDB)	$\delta^{13}C$ stdev	$\delta^{18}O$ CO_2 (SMOW)	$\delta^{18}O$ calcite (PDB)	$\delta^{18}O$ stdev	δ_{47} (v. Oz)	δ_{47} stdev	Δ_{47} (v. Oz)	Δ_{47} stdev	Δ_{47} sterror	δ_{48} (v. Oz)	Δ_{48} (v. Oz)	Δ_{48} stdev	HG correct. Δ_{47}	stretch correct. Δ_{47}	acid dig. correct. Δ_{47}
Carrara Marble, Analytical Session 1, 8/31/2010-9/11/2010																
8/30/10	2.348	0.007	37.356	-1.893	0.035	17.722	0.027	-0.406	0.028	0.010	30.564	6.139	0.847	0.225	0.232	0.312
8/31/10	2.352	0.002	37.421	4.471	0.004	17.818	0.028	-0.378	0.026	0.008	30.813	6.257	0.379	0.251	0.259	0.339
9/1/10	2.263	0.003	37.344	-1.904	0.004	17.661	0.015	-0.372	0.023	0.008	30.435	6.037	0.334	0.259	0.268	0.348
9/2/10	2.329	0.002	37.445	-1.807	0.003	17.864	0.017	-0.336	0.040	0.014	31.307	6.691	0.490	0.293	0.303	0.383
9/4/10	2.322	0.003	37.369	-1.881	0.002	17.738	0.043	-0.377	0.044	0.008	30.896	6.439	0.205	0.253	0.262	0.342
9/5/10	2.318	0.003	37.327	-1.921	0.003	17.683	0.018	-0.386	0.018	0.007	30.898	6.522	0.351	0.244	0.253	0.333
9/8/10	2.346	0.003	37.381	-1.869	0.005	17.808	0.022	-0.343	0.040	0.014	31.397	6.904	0.216	0.286	0.296	0.376
9/9/10	2.346	0.003	37.403	-1.848	0.005	17.816	0.016	-0.357	0.034	0.012	31.413	6.878	0.372	0.272	0.281	0.361
9/11/10	2.339	0.002	37.400	-1.850	0.005	17.804	0.029	-0.359	0.036	0.013	31.542	7.009	0.251	0.270	0.279	0.359
9/11/10	2.343	0.002	37.478	-1.775	0.005	17.875	0.030	-0.370	0.030	0.011	31.651	6.964	0.274	0.259	0.267	0.347
9/13/10	2.308	0.002	37.408	-1.843	0.004	17.759	0.0187	-0.3811	0.0171	0.0061	31.764	7.210	0.453	0.249	0.257	0.337
															average:	*0.349*
															stdev:	*0.020*
Carmel Calcite, Analytical Session 1, 8/31/2010-9/11/2010																
8/30/10	-2.108	0.003	35.141	-4.024	0.006	11.395	0.009	-0.173	0.026	0.009	25.784	5.779	0.300	0.526	0.542	0.622
8/31/10	-2.223	0.003	35.056	-4.106	0.003	11.225	0.019	-0.146	0.023	0.008	25.148	5.321	0.311	0.555	0.572	0.652
8/31/10	-2.151	0.002	35.098	-4.065	0.003	11.325	0.029	-0.158	0.030	0.011	25.075	5.167	0.304	0.541	0.558	0.638
9/2/10	-2.204	0.002	34.964	-4.195	0.007	11.169	0.023	-0.129	0.057	0.020	26.233	6.563	1.932	0.572	0.590	0.670
9/3/10	-2.217	0.003	35.060	-4.102	0.004	11.258	0.014	-0.123	0.029	0.010	25.115	5.281	0.342	0.577	0.595	0.675
9/3/10	-1.160	0.003	30.190	-8.788	0.003	7.352	0.013	-0.206	0.034	0.012	13.533	3.327	0.237	0.535	0.552	0.632
9/4/10	-2.180	0.004	35.078	-4.085	0.004	11.268	0.022	-0.167	0.026	0.009	25.841	5.957	0.146	0.533	0.550	0.630
9/5/10	-2.153	0.004	35.047	-4.115	0.004	11.279	0.022	-0.151	0.037	0.013	25.412	5.596	0.440	0.548	0.566	0.646
9/7/10	-2.195	0.008	34.791	-4.361	0.012	10.952	0.017	-0.183	0.026	0.009	24.899	5.589	0.373	0.521	0.537	0.617
9/8/10	-2.131	0.003	35.105	-4.059	0.009	11.352	0.019	-0.157	0.036	0.013	25.599	5.668	0.428	0.542	0.559	0.639
9/10/10	-2.135	0.004	35.167	-3.999	0.004	11.398	0.028	-0.169	0.045	0.016	25.956	5.897	0.253	0.530	0.546	0.626
9/12/10	-2.143	0.003	35.187	-3.980	0.003	11.447	0.022	-0.133	0.029	0.010	25.944	5.846	0.439	0.565	0.583	0.663
															average:	*0.643*
															stdev:	*0.019*

Table A2
(continued)

date	$\delta^{13}C$ (PDB)	$\delta^{13}C$ stdev	$\delta^{18}O$ CO_2 (SMOW)	$\delta^{18}O$ calcite (PDB)	$\delta^{18}O$ stdev	δ_{47} (v. Oz)	δ_{47} stdev	Δ_{47} (v. Oz)	Δ_{47} stdev	Δ_{47} sterror	δ_{48} (v. Oz)	Δ_{48} (v. Oz)	Δ_{48} stdev	HG correct. Δ_{47}	stretch correct. Δ_{47}	acid dig. correct. Δ_{47}
Carrara Marble, Analytical Session 2, 8/21/2011-8/28/2011																
8/20/11	2.354	0.003	37.316	-1.931	0.006	17.692	0.025	-0.402	0.030	0.011	28.235	3.943	0.213	0.243	0.264	0.344
8/21/11	2.352	0.003	37.334	-1.914	0.005	17.717	0.019	-0.392	0.026	0.009	28.430	4.098	0.186	0.253	0.275	0.355
8/22/11	2.354	0.003	37.346	-1.903	0.006	17.738	0.025	-0.385	0.014	0.005	28.383	4.030	0.129	0.260	0.282	0.362
8/25/11	2.357	0.003	37.340	-1.908	0.012	17.741	0.022	-0.379	0.030	0.011	28.548	4.202	0.184	0.265	0.289	0.369
8/26/11	2.353	0.005	37.325	-1.923	0.026	17.724	0.027	-0.378	0.028	0.010	28.655	4.336	0.191	0.266	0.290	0.370
8/28/11	2.360	0.006	37.404	-1.847	0.034	17.804	0.061	-0.383	0.033	0.012	28.830	4.355	0.174	0.261	0.284	0.364
8/29/11	2.375	0.002	37.380	-1.870	0.009	17.787	0.022	-0.381	0.022	0.008	28.637	4.192	0.154	0.263	0.286	0.366
8/29/11	2.380	0.004	37.321	-1.927	0.004	17.719	0.023	-0.394	0.026	0.009	28.512	4.185	0.101	0.251	0.272	0.352
8/30/11	2.321	0.002	37.407	-1.844	0.006	17.738	0.026	-0.404	0.027	0.009	28.878	4.376	0.122	0.240	0.261	0.341
9/1/11	2.228	0.003	37.260	-1.986	0.004	17.496	0.031	-0.408	0.026	0.009	28.635	4.424	0.199	0.238	0.259	0.339
9/3/11	2.359	0.004	37.342	-1.906	0.003	17.729	0.024	-0.385	0.018	0.006	28.884	4.506	0.139	0.259	0.282	0.362
9/4/11	2.357	0.002	37.371	-1.879	0.004	17.750	0.036	-0.392	0.034	0.012	28.907	4.474	0.079	0.253	0.275	0.355
9/6/11	2.378	0.003	37.351	-1.898	0.004	17.752	0.009	-0.390	0.019	0.007	28.759	4.368	0.071	0.254	0.277	0.357
9/7/11	2.381	0.004	37.355	-1.894	0.010	17.760	0.017	-0.389	0.011	0.004	28.928	4.525	0.172	0.255	0.277	0.357
9/8/11	2.382	0.004	37.318	-1.929	0.006	17.686	0.022	-0.427	0.019	0.007	28.703	4.376	0.105	0.218	0.237	0.317
9/9/11	2.382	0.003	37.264	-1.982	0.003	17.638	0.028	-0.421	0.025	0.009	28.801	4.577	0.176	0.224	0.244	0.324
9/10/11	2.380	0.004	37.335	-1.913	0.003	17.738	0.011	-0.390	0.023	0.008	28.988	4.623	0.125	0.255	0.277	0.357
9/10/11	2.376	0.003	37.313	-1.935	0.004	17.715	0.021	-0.387	0.030	0.011	28.840	4.521	0.150	0.258	0.280	0.360
9/11/11	2.380	0.002	37.384	-1.866	0.004	17.845	0.019	-0.334	0.024	0.009	29.188	4.723	0.164	0.310	0.337	0.417
9/12/11	2.384	0.003	37.374	-1.876	0.003	17.765	0.009	-0.406	0.027	0.009	29.206	4.760	0.151	0.239	0.259	0.339
															average:	0.355
															stdev:	0.020
TV-01 Calcite, Analytical Session 2, 8/21/2011-8/28/2011:																
8/21/11	2.395	0.003	30.494	-8.496	0.007	11.156	0.020	-0.158	0.029	0.010	12.547	1.746	0.133	0.535	0.582	0.662
8/21/11	2.494	0.002	30.493	-8.496	0.007	11.267	0.017	-0.144	0.028	0.010	12.649	1.847	0.227	0.549	0.597	0.677
8/22/11	2.590	0.004	30.439	-8.549	0.008	11.323	0.015	-0.127	0.028	0.010	12.256	1.563	0.129	0.566	0.615	0.695
8/23/11	2.596	0.004	30.436	-8.551	0.021	11.287	0.112	-0.166	0.027	0.009	12.464	1.773	0.162	0.527	0.573	0.653
8/26/11	2.545	0.003	30.417	-8.569	0.007	11.227	0.021	-0.158	0.016	0.006	12.578	1.923	0.185	0.535	0.582	0.662
8/27/11	2.622	0.005	30.382	-8.603	0.012	11.255	0.022	-0.169	0.014	0.005	12.472	1.888	0.181	0.524	0.570	0.650
8/29/11	2.656	0.003	30.418	-8.569	0.004	11.308	0.010	-0.175	0.012	0.004	12.717	2.040	0.120	0.517	0.562	0.642
8/29/11	2.660	0.002	30.444	-8.543	0.007	11.342	0.024	-0.172	0.023	0.008	12.606	1.879	0.252	0.520	0.566	0.646

Table A2
(continued)

date	$\delta^{13}C$ (PDB)	$\delta^{13}C$ stdev	$\delta^{18}O$ CO_2 (SMOW)	$\delta^{18}O$ calcite (PDB)	$\delta^{18}O$ stdev	δ_{47} (v. Oz)	δ_{47} stdev	Δ_{47} (v. Oz)	Δ_{47} stdev	Δ_{47} sterror	δ_{48} (v. Oz)	Δ_{48} (v. Oz)	Δ_{48} stdev	HG correct. Δ_{47}	stretch correct. Δ_{47}	acid dig. correct. Δ_{47}
TV-01 Calcite, Analytical Session 2, 8/21/2011-8/28/2011:																
8/31/11	2.393	0.002	30.689	-8.308	0.004	11.341	0.026	-0.159	0.028	0.010	13.307	2.098	0.095	0.534	0.580	0.660
9/2/11	2.646	0.002	30.440	-8.547	0.004	11.335	0.027	-0.161	0.026	0.009	12.801	2.080	0.244	0.532	0.578	0.658
9/6/11	2.603	0.003	30.492	-8.497	0.007	11.349	0.022	-0.158	0.036	0.013	12.874	2.052	0.234	0.535	0.581	0.661
9/8/11	2.543	0.004	30.387	-8.598	0.006	11.159	0.020	-0.183	0.021	0.008	12.450	1.837	0.157	0.510	0.555	0.635
9/8/11	2.593	0.004	30.370	-8.614	0.004	11.185	0.012	-0.189	0.028	0.010	12.464	1.883	0.155	0.505	0.549	0.629
9/8/11	2.618	0.004	30.477	-8.511	0.008	11.303	0.020	-0.203	0.021	0.007	12.682	1.890	0.192	0.490	0.533	0.613
9/10/11	2.562	0.005	30.422	-8.564	0.003	11.227	0.021	-0.169	0.027	0.009	12.831	2.145	0.163	0.524	0.570	0.650
9/10/11	2.575	0.003	30.407	-8.579	0.003	11.225	0.022	-0.169	0.028	0.010	12.764	2.109	0.184	0.525	0.571	0.651
9/12/11	2.570	0.003	30.401	-8.585	0.005	11.212	0.014	-0.171	0.041	0.015	12.737	2.092	0.118	0.522	0.567	0.647
															average:	0.652
															stdev:	0.018
NBS-19 Calcite, Analytical Session 2, 8/21/2011-8/28/2011:																
8/24/11	2.053	0.004	36.963	-2.272	0.016	17.075	0.029	-0.371	0.037	0.013	27.670	4.076	0.139	0.278	0.303	0.383
8/27/11	2.047	0.004	36.942	-2.292	0.008	17.035	0.026	-0.384	0.022	0.008	27.750	4.195	0.237	0.266	0.289	0.369
8/28/11	2.055	0.004	36.974	-2.261	0.014	17.080	0.025	-0.379	0.027	0.010	27.854	4.235	0.123	0.271	0.294	0.374
															average:	0.375
															stdev:	0.007

All values are reported in ‰. "Oz" refers to working reference gas by Oztech.

TABLE A3

Summary of transfer function data for the absolute reference frame

sample	analytical session	measured Δ_{47} (‰)	accepted Δ_{47} (‰)	source of accepted value
HG	Sessions 1 & 2	0.000	0.0266	Dennis and others, 2011
Carrara	Session 1	0.349	0.395	Dennis and others, 2011
Carmel	Session 1	0.643	0.705	H. Affek, pers. comm. 2012
Carrara	Session 2	0.355	0.395	Dennis and others, 2011
TV-01	Session 2	0.652	0.713	J. Eiler, pers. comm. 2012
NBS-19	Session 2	0.375	0.392	Dennis and others, 2011

Transfer function from Caltech reference frame to absolute reference frame: Δ_{47}, ARF = 1.0567 (Δ_{47}, Caltech) + 0.0197 ($R^2 = 0.99777$).

standardization, which uses assumed Δ_{47} values for these 1000 °C heated gases and measured and assumed Δ_{47} values for carbonate standards. Table A2 presents the isotopic results for the carbonate standards (Carrara marble, TV-01 calcite, and Carmel calcite). Table A3 summarizes the information derived from the data in tables A1 and A2, along with the accepted Δ_{47} values for these samples in the absolute reference frame. The transfer function from the Caltech reference frame to the absolute reference frame did not change between analytical sessions 1 and 2, so a single transfer function is reported in table A3 and used to reference the results presented in table 1.

REFERENCES

Anderson, M. P., 2005, Heat as a ground water tracer: Groundwater, v. 43, n. 6, p. 951–968, http://dx.doi.org/10.1111/j.1745-6584.2005.00052.x

Antonellini, M., and Aydin, A., 1994, Effect of faulting on fluid flow in porous sandstones: petrophysical properties: AAPG Bulletin, v. 78, n. 3, p. 355–377.

Aydin, A., 2000, Fractures, faults, and hydrocarbon entrapment, migration and flow: Marine and Petroleum Geology, v. 17, n. 7, p. 797–814, http://dx.doi.org/10.1016/S0264-8172(00)00020-9

Aydin, A., and Johnson, A. M., 1978, Development of faults as zones of deformation bands and as slip surfaces in sandstone: Pure and Applied Geophysics, v. 116, n. 4–5, p. 931–942, http://dx.doi.org/10.1007/BF00876547

Boggs, S., and Krinsley, D., 2006, Application of cathodoluminescence imaging to the study of sedimentary rocks: Cambridge, Cambridge University Press, 165 p.

Boles, J. R., Eichhubl, P., Garven, G., and Chen, J., 2004, Evolution of a hydrocarbon migration pathway along basin-bounding faults: Evidence from fault cement: AAPG Bulletin, v. 88, p. 947–970, http://dx.doi.org/10.1306/02090403040

Caine, J. S., Evans, J. P., and Forster, C. B., 1996, Fault zone architecture and permeability structure: Geology, v. 24, n. 11, p. 1025–1028, http://dx.doi.org/10.1130/0091-7613(1996)024(1025:FZAAPS)2.3.CO;2

Chan, M. A., Parry, W. T., and Bowman, J. R., 2000, Diagenetic hematite and manganese oxides and fault-related fluid flow in Jurassic sandstones, southeastern Utah: AAPG Bulletin, v. 84, n. 9, p. 1281–1310, http://dx.doi.org/10.1306/A9673E82-1738-11D7-8645000102C1865D

Davatzes, N., and Aydin, A., 2003, Overprinting faulting mechanisms in high porosity sandstones of SE Utah: Journal of Structural Geology, v. 25, n. 11, p. 1795–1813, http://dx.doi.org/10.1016/S0191-8141(03)00043-9

Davatzes, N. C., Aydin, A., and Eichhubl, P., 2003, Overprinting faulting mechanisms during the development of multiple fault sets in sandstone, Chimney Rock fault array, Utah, USA: Tectonophysics, v. 363, n. 1–2, p. 1–18, http://dx.doi.org/10.1016/S0040-1951(02)00647-9

Davatzes, N. C., Eichhubl, P., and Aydin, A., 2005, Structural evolution of fault zones in sandstone by multiple deformation mechanisms: Moab fault, southeast Utah: Geological Society of America Bulletin, v. 117, n. 1–2, p. 135–148, http://dx.doi.org/10.1130/B25473.1

Dennis, K. J., and Schrag, D. P., 2010, Clumped isotope thermometry of carbonatites as an indicator of diagenetic alteration: Geochimica et Cosmochimica Acta, v. 74, n. 15, p. 4110–4122, http://dx.doi.org/10.1016/j.gca.2010.04.005

Dennis, K. J., Affek, H. P., Passey, B. H., Schrag, D. P., and Eiler, J. M., 2011. Defining an absolute reference frame for "clumped" isotope studies of CO_2: Geochimica et Cosmochimica Acta, v. 75, n. 22, p. 7117–7131, http://dx.doi.org/10.1016/j.gca.2011.09.025

Doelling, H., 1985, Geologic map of Arches National Park and vicinity, Grand County, Utah: Salt Lake City, Utah, Utah Geological and Mineral Survey, Map 74, scale 1:50,000.

——— 2002, Geologic map of the Moab 7.5′ quadrangle, Grand County, Utah: Salt Lake City, Utah, Utah Geological Survey, Utah Department of Natural Resources.

Eichhubl, P., Greene, H. G., Naehr, T., and Maher, N., 2000, Structural control of fluid flow: offshore fluid

seepage in the Santa Barbara Basin, California: Journal of Geochemical Exploration, v. 69–70, p. 545–549, http://dx.doi.org/10.1016/S0375-6742(00)00107-2

Eichhubl, P., Taylor, W. L., Pollard, D. D., and Aydin, A., 2004: Paleo-fluid flow and deformation in the Aztec sandstone at the Valley of Fire, Nevada—evidence for the coupling of hydrogeologic, diagenetic, and tectonic processes: Geological Society of America Bulletin, v. 116, n. 9–10, p. 1120–1136, http://dx.doi.org/10.1130/B25446.1

Eichhubl, P., Davatz, N. C., and Becker, S. P., 2009, Structural and diagenetic control of fluid migration and cementation along the Moab fault, Utah: AAPG Bulletin, v. 93, n. 5, p. 653–681, http://dx.doi.org/10.1306/02180908080

Eiler, J. M., 2007, "Clumped-isotope" geochemistry—The study of naturally-occurring, multiply-substituted isotopologues: Earth and Planetary Science Letters, v. 262, n. 3–4, p. 309–327, http://dx.doi.org/10.1016/j.epsl.2007.08.020

Fossen, H., Johansen, T. E. S., Hesthammer, J., and Rotevatn, A., 2005, Fault interaction in porous sandstone and implications for reservoir management; examples from southern Utah: AAPG Bulletin, v. 89, n. 12, p. 1593–1606, http://dx.doi.org/10.1306/07290505041

Fossen, H., Schultz, R. A., Shipton, Z. K., and Mair, K., 2007, Deformation bands in sandstone: a review: Journal of the Geological Society, London, v. 164, n. 4, p. 755–769, http://dx.doi.org/10.1144/0016-76492006-036

Foxford, K. A., Garden, I. R., Guscott, S. C., Burley, S. D., Lewis, J. J., Walsh, J. J., and Watterson, J., 1996, The field geology of the Moab fault, *in* Huffman, A. C., Jr., Lund, W. R., and Godwin, L. H., editors, Geology and Resources of the Paradox Basin: Utah Geological Association Guidebook, v. 25, p. 265–283.

Foxford, K. A., Walsh, J. J., Watterson, J., Garden, I. R., Guscott, S. C., and Burley, S. D., 1998, Structure and content of the Moab fault zone, Utah, USA, and its implications for fault seal prediction: Geological Society, London, Special Publications, v. 147, p. 87–103, http://dx.doi.org/10.1144/GSL.SP.1998.147.01.06

Garden, I. R., Guscott, S. C., Burley, S. D., Foxford, K. A., Walsh, J. J., and Marshall, J., 2001, An exhumed palaeo-hydrocarbon migration fairway in a faulted carrier system, Entrada Sandstone of SE Utah, USA: Geofluids, v. 1, n. 3, p. 195–213, http://dx.doi.org/10.1046/j.1468-8123.2001.00018.x

Ghosh, P., Adkins, J., Affek, H., Balta, B., Guo, W., Schauble, E. A., Schrag, D., and Eiler, J. M., 2006, ^{13}C–^{18}O bonds in carbonate minerals: A new kind of paleothermometer: Geochimica et Cosmochimica Acta, v. 70, n. 5, p. 1439–1456, http://dx.doi.org/10.1016/j.gca.2005.11.014

Guo, W., Mosenfelder, J. L., Goddard, W. A., III, and Eiler, J. M., 2009, Isotopic fractionations associated with phosphoric acid digestion of carbonate minerals: Insights from first-principles theoretical modeling and clumped isotope measurements: Geochimica et Cosmochimica Acta 73, n. 24, p. 7203–7225, http://dx.doi.org/10.1016/j.gca.2009.05.071

Huntington, K. W., Eiler, J. M., Affek, H. P., Guo, W., Bonifacie, M., Yeung, L. Y., Thiagarajan, N., Passey, B., Tripati, A., Daëron, M., and Came, R., 2009, Methods and limitations of "clumped" CO_2 isotope (Δ_{47}) analysis by gas-source isotope ratio mass spectrometry: Journal of Mass Spectrometry, v. 44, n. 9, p. 1318–1329, http://dx.doi.org/10.1002/jms.1614

Huntington, K. W., Budd, D. A., Wernicke, B. P., and Eiler, J. M., 2011, Use of clumped-isotope thermometry to constrain the crystallization temperature of diagenetic calcite: Journal of Sedimentary Research, v. 81, n. 9, p. 656–669, http://dx.doi.org/10.2110/jsr.2011.51

Ingebritsen, S. E., Sanford, W. E., and Neuzil, C. E., 2006, Groundwater in Geologic Processes, 2nd edition: Cambridge, Cambridge University Press, 536 p.

Johansen, T. E. S., and Fossen, H., 2008, Internal deformation of fault damage zones in interbedded siliciclastic rocks, *in* Wibberley, C. A. J., Kurtz, W., Imber, J., Holdsworth, R. E., and Collettini, C., editors, The internal structure of fault zones: Implications for mechanical and fluid-flow properties: Geological Society, London, Special Publications, v. 299, p. 35–56, http://dx.doi.org/10.1144/SP299.3

Johansen, T. E. S., Fossen, H., and Kluge, R. 2005, The impact of syn-faulting porosity reduction on damage zone architecture in porous sandstone; an outcrop example from the Moab Fault, Utah: Journal of Structural Geology, v. 27, n. 8, p. 1469–1485, http://dx.doi.org/10.1016/j.jsg.2005.01.014

Kim, S.-T., and O'Neil, J. R., 1997, Equilibrium and nonequilibrium oxygen isotope effects in synthetic carbonates: Geochimica et Cosmochimica Acta, v. 61, n. 16, p. 3461–3475, http://dx.doi.org/10.1016/S0016-7037(97)00169-5

Laubach, S. E., and Ward, M. E., 2006, Diagenesis in porosity evolution of opening-mode fractures, Middle Triassic to Lower Jurassic La Boca Formation, NE Mexico: Tectonophysics, v. 419, n. 1–4, p. 75–97, http://dx.doi.org/10.1016/j.tecto.2006.03.020

Laubach, S. E., Olson, J. E., and Eichhubl, P., 2009, Fracture diagenesis and producibility in tight gas sandstones, *in* Carr, T., d'Agostino, T., Ambrose, W., Pashin, J., and Rosen, N. C., editors, Unconventional Energy Resources: Making the Unconventional Conventional, 29th Annual GCSSEPM Foundation Annual Bob F. Perkins Research Conference Proceedings, v. 29, p. 483–499.

Long, J. C. S., Aydin, A., Brown, S. R., Einstein, H. H., Hestir, K., Hsieh, P. A., Myer, L. R., Nolte, K. G., Norton, D. L., Olsson, O. L., Paillet, F. L., Smith, J. L., and Thomsen, L., 1996, Rock Fractures and Fluid Flow: Contemporary Understanding and Applications: Washington, D.C., National Academy Press, 551 p.

Morrison, S. J., and Parry, W. T., 1986, Formation of carbonate-sulfate veins associated with copper ore deposits from saline basin brines, Lisbon Valley, Utah; fluid inclusion and isotopic evidence: Economic Geology, v. 81, n. 8, p. 1853–1866, http://dx.doi.org/10.2113/gsecongeo.81.8.1853

Myers, R., and Aydin, A., 2004, The evolution of faults formed by shearing across joint zones in sandstone: Journal of Structural Geology, v. 26, n. 4, p. 947–966, http://dx.doi.org/10.1016/j.jsg.2003.07.008

Nuccio, V. F., and Condon, S. M., 1996, Burial and thermal history of the Paradox Basin, Utah and Colorado,

and petroleum potential of the middle Pennsylvanian Paradox Formation: U.S. Geological Survey Bulletin 2000-0, 01–041 p.

Passey, B. H., Levin, N. E., Cerling, T. E., Brown, F. H., and Eiler, J. M., 2010, High-temperature environments of human evolution in east Africa based on bond ordering in paleosol carbonates: Proceedings of the National Academy of Sciences, v. 107, n. 25, p. 11245–11249, http://dx.doi.org/10.1073/pnas.1001824107

Pevear, D. R., Vrolijk, P. L., and Lomgstaffe, F. J., 1997, Timing of Moab fault displacement and fluid movement integrated with burial history using radiogenic and stable isotopes, *in* Contributions to the Second International Conference on Fluid Evolution, Migration and Interaction in Sedimentary Basins and Orogenic Belts: Geofluids II Conference, The Queen's University of Belfast, Belfast, Northern Ireland, Geofluids II Extended Abstracts, p. 42–45.

Schauble, E. A., Ghosh, P., and Eiler, J. M., 2006, Preferential formation of ^{13}C–^{18}O bonds in carbonate minerals, estimated using first-principles lattice dynamics: Geochimica et Cosmochimica Acta, v. 70, n. 10, p. 2510–2529, http://dx.doi.org/10.1016/j.gca.2006.02.011

Solum, J. G., van der Pluijm, B. A., and Peacor, D. R., 2005, Neocrystallization, fabrics and age of clay minerals from an exposure of the Moab Fault, Utah: Journal of Structural Geology, v. 27, n. 9, p. 1563–1576, http://dx.doi.org/10.1016/j.jsg.2005.05.002

Solum, J. G., Davatzes, N. C., and Lockner, D. A., 2010, Fault-related clay authigenesis along the Moab Fault: Implications for calculations of fault rock composition and mechanical and hydrologic fault zone properties: Journal of Structural Geology, v. 32, n. 12, p. 1899–1911, http://dx.doi.org/10.1016/j.jsg.2010.07.009

Spangler, L. E., Naftz, D. L., and Peterman, Z. E., 1996, Hydrology, chemical quality, and characterization of salinity in the Navajo aquifer in and near the Greater Aneth Oil Field, San Juan County, Utah: U.S. Geological Survey Water-Resources Investigations Report 96-4155, 90 p.

Swanson, E. M., Wernicke, B. P., Eiler, J. M., and Losh, S., 2012, Temperatures and fluids on faults based on carbonate clumped–isotope thermometry: American Journal of Science, v. 312, n. 1, p. 1–21, http://dx.doi.org/10.2475/01.2012.01

Tripati, A. K., Eagle, R. A., Thiagarajan, N., Gagnon, A. C., Bauch, H., Halloran, P. R., and Eiler, J. M., 2010, ^{13}C–^{18}O isotope signatures and "clumped isotope" thermometry in foraminifera and coccoliths: Geochimica et Cosmochimica Acta, v. 74, n. 20, p. 5697–5717, http://dx.doi.org/10.1016/j.gca.2010.07.006

Vrolijk, P., and van der Pluijm, B. A., 1999, Clay gouge: Journal of Structural Geology, v. 21, n. 8–9, p. 1039–1048, http://dx.doi.org/10.1016/S0191-8141(99)00103-0